# Critical role of the coupling between the octahedral rotation and *A*-site ionic displacements in PbZrO₃-based antiferroelectric materials investigated by *in situ* neutron diffraction

Teng Lu,[1] Andrew J. Studer,[2] Dehong Yu,[2] Ray L. Withers,[1] Yujun Feng,[3] Hua Chen,[4] S. S. Islam,[5] Zhuo Xu,[3] and Yun Liu[1,*]

[1]*Research School of Chemistry, The Australian National University, ACT 2601, Australia*
[2]*Australian Centre for Neutron Scattering, Australian Nuclear Science and Technology Organisation, Lucas Height, NSW 2234, Australia*
[3]*Electronic Materials Research Laboratory, Xi'an Jiaotong University, Xi'an 710049, Shaanxi, China*
[4]*Centre for Advanced Microscopy, The Australian National University, ACT 2601, Australia*
[5]*Nano Sensor Research Laboratory, Jamia Millia Islamia, New Delhi 110025, India*

This *in situ* neutron-diffraction study on antiferroelectric (AFE) Pb$_{0.99}$(Nb$_{0.02}$Zr$_{0.65}$Sn$_{0.28}$Ti$_{0.05}$)O$_3$ polycrystalline materials describes systematic structural and associated preferred orientation changes as a function of applied electric field and temperature. It is found that the pristine AFE phase can be poled into the metastable ferroelectric (FE) phase at room temperature. At this stage, both AFE and FE phases consist of modes associated with octahedral rotation and *A*-site ionic displacements. The temperature-induced phase transition indicates that the octahedral rotation and ionic displacements are weakly coupled in the room-temperature FE phase and decoupled in the high-temperature FE phase. However, both temperature and *E*-field-induced phase transitions between the AFE and high-temperature FE phase demonstrate the critical role of coupling between octahedral rotation and *A*-site ionic displacements in stabilizing the AFE structure, which provides not only experimental evidence to support previous theoretical calculations, but also an insight into the design and development of AFE materials. Moreover, the associated preferred orientation evolution in both AFE and FE phases is studied during the phase transitions. It is found that the formation of the preferred orientation can be controlled to tune the samples' FE and AFE properties.

## I. INTRODUCTION

Antiferroelectric (AFE) materials such as PbZrO₃ (PZO) and PZO-based materials exhibit many distinctive and useful properties, such as large electric-field (*E*-field) -induced strains, double-polarization–electric-field (*P-E*) hysteresis loops, and thermal/mechanical depolarization. These distinctive properties have many possible applications and have already led to the development of various devices, including potential generators, energy storage devices, and sensors [1–7]. The origin of these useful properties is associated with the distinctive structural transition between the AFE and FE phases induced by external stimuli such as *E*-field, mechanical force, and temperature [5,8–11]. From the Kittel two-sublattice model, the AFE-FE phase transition could be attributed to the switching of the sign of one of the two sets of antiparallel, off-center atomic displacements, i.e., the resultant antiparallel dipoles of the AFE phase [shown in Fig. 1(a)] [12]. In reality, the AFE-FE transition is considerably more complicated. Recently, the origin of antiferroelectricity in PZO and PZO-related materials has been under intensive discussion, particularly from the soft mode and overall energy points of view [13–18].

Relative to an undistorted, parent perovskite (subscript p), PZO has a $\sqrt{2} \times 2\sqrt{2} \times 2$ unit cell and space-group symmetry of *Pbam* under ambient conditions. A symmetry mode decomposition [19,20] of, for example, Corker *et al.*'s structure refinement [21] shows that the ground state of PZO is dominated by two large-amplitude primary modes. The first mode is associated with the modulation wave vector $\mathbf{q}_1 = [1/4,1/4,0]_p{}^*$

(of $\Sigma_2$ symmetry) and results in antiparallel displacements of *A*-site Pb²⁺ and the neighboring apical O²⁻ ions along the resultant $\boldsymbol{a}$, or $[1\text{-}10]_p$, directions [of magnitudes 0.277 and 0.215 Å, respectively; see Fig. 1(a)]. These large-amplitude displacements give rise to $(010) \equiv (110)_p$ slabs (two octahedra wide) polarized along the $\pm\boldsymbol{a}$ direction. It is evident that the $\mathbf{q}_1$ mode is responsible for the antiferroelectricity in PZO, hereafter referred to as the AFE mode. The second soft mode is a conventional octahedral rotation, or antiferrodistortive (AFD) mode around the resultant $\boldsymbol{a}$, or $\boldsymbol{a}_p - \boldsymbol{b}_p$, direction, associated with the modulation wave vector $\mathbf{q}_2 = 1/2[111]_p{}^*$ (of $R_4$ symmetry), as shown in Fig. 1(b). Obviously, the distorted structure induced by this octahedral rotation mode presents higher symmetry than the ground state of PZO. The resultant lattice vectors have the following relationship with those of the parent perovskite: $\boldsymbol{a} \equiv \boldsymbol{a}_p - \boldsymbol{b}_p, \boldsymbol{b} \equiv \boldsymbol{a}_p + \boldsymbol{b}_p$, and $\boldsymbol{c} \equiv 2\boldsymbol{c}_p$. It is noted that an additional, much smaller amplitude, the secondary mode (of $S_4$ symmetry) associated with the modulation wave vector $\mathbf{q}_3 = \mathbf{q}_2 - \mathbf{q}_1 = 1/4[112]_p{}^*$, and induced "via a cooperative trilinear coupling" with the $\mathbf{q}_1$ and $\mathbf{q}_2$ modes, has recently been reported as being essential to the stabilization of the overall PZO structure [16].

Ideally, when switching the AFE phase into the FE phase by applying the *E*-field, the AFE mode will totally disappear and all the *A*-site Pb²⁺ are forced to align in the same direction of the *E*-field. That is, rather than the antiparallel displacements associated with the $\mathbf{q}_1$ mode, *A*-site ions displace in the same direction, correlated with the zone center, $\mathbf{q} = [000]_p{}^*$, mode (FE mode) [18]. In PZO, especially for the polycrystalline materials, the large critical *E*-field for an AFE-to-FE phase transition rules out potential applications, thus the perovskite *B*-site modified Pb(Zr,Sn,Ti)O₃ (PZST) ternary systems have been developed to overcome this limitation

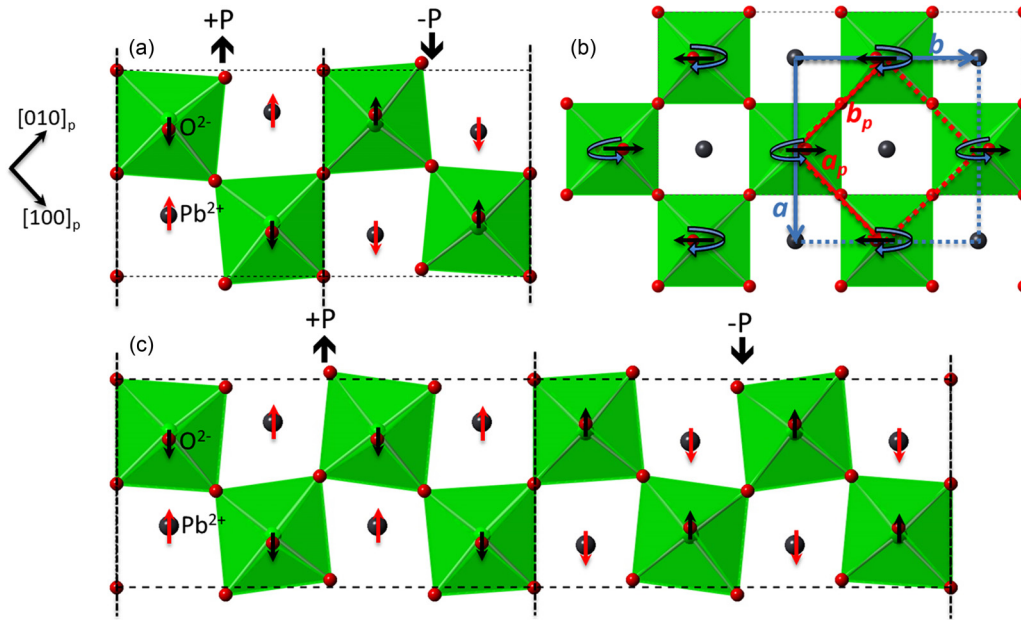*Corresponding author: yun.liu@anu.edu.au

FIG. 1. (a) The distorted structure induced by $\mathbf{q}_1 = {}^1/_4 [110]_p{}^*$ of the PZO structure in projection along $\mathbf{c}$. The resultant $\mathbf{a} \equiv [1\text{-}10]_p$ and $\mathbf{b} \equiv [220]_p$ are shown by the lighter dashed lines, while the heavier dashed vertical lines separate the two octahedral layer wide regions, which are alternately polarized up and down. (b) The distorted structure induced by $\mathbf{q}_2 = {}^1/_2 [111]_p{}^*$, the octahedral tilting mode, and the resultant lattice vectors $\mathbf{a}$ and $\mathbf{b}$ (blue line) are described by the lattice vectors of parent perovskite structure (red line) as follows: $\mathbf{a} = \mathbf{a}_p - \mathbf{b}_p$; $\mathbf{b} = \mathbf{a}_p + \mathbf{b}_p$. (c) A suggested schematic structure for a proposed $\mathbf{q} = 1/8[110]_p{}^*$ AFE-type mode. Here the heavier dashed vertical lines separate four octahedral layer wide regions, which are again alternately polarized up and down, respectively. Note that the oxygens on these lines do not move in both (a) and (c).

[22–24]. Intriguingly, *B*-site modified PZO has been shown via electron diffraction [25–29] to change the modulation wave vector of the AFE mode from $\mathbf{q}_1 = 1/4[110]_p{}^*$ to $\mathbf{q}_1 = \gamma[110]_p{}^*$, where $\gamma$ is significantly reduced from the parent PZO value of 1/4 to $1/6 \leqslant \gamma \leqslant 1/8$ (see Table 1 in Ref. [29]). Tan *et al.* [28,29], following Sawaguchi *et al.* [30], have proposed a simplified Pb shift-only model to explain the antiferroelectricity observed in these doped PZST material systems. Figure 1(c) shows a somewhat more sophisticated model for these La/Nb modified PZST materials, based on the AFE mode discussed above, for $\gamma = 1/8$.

Clearly, following Sawaguchi *et al.* [30] and Tan *et al.* [28,29], it is not difficult to generalize this model for other commensurate values ($1/\gamma$ is an integer) or, in general, an incommensurate value. Lowering $\gamma$ from its 1/4 value for PZO, for example, to 1/8 simply increases the average distance between the boundaries along $\mathbf{b} \equiv [110]_p$ [the heavier vertical dashed lines in Figs. 1(a) and 1(c)]. In parent PZO, where $\gamma = 1/4$, only two *A*-site $Pb^{2+}$ ions are involved in one FE slab region, while for $\gamma = 1/8$, the number of $Pb^{2+}$ involved in one FE slab [cf. Figs. 1(a) with 1(c)] is four. It is not hard to see that although the modulation wave vector of the $\mathbf{q}_1$ mode can move along the $\Sigma$ line in the first Brillouin zone of the parent perovskite structure, it is still responsible for the resultant antiferroelectricity.

Theoretical calculations [14,17] suggest the collaborative coupling between the *A*-site ionic displacements, $\mathbf{q}_1$, and the octahedral rotation, $\mathbf{q}_2$, mode(s) that can lead to "*hybrid* normal modes," which can explain the experimental fact that both modes condense simultaneously at a certain temperature in the case of PZO as well as the existence of a soft phonon branch

along the $\gamma[110]_p{}^*$ reciprocal space direction. The calculations [14,31] also point out that the coupling between the AFD mode and the FE mode is present in a competitive rather than a collaborative nature. The AFE-FE phase transition provides an experimental case to compare the different nature of the coupling between the *A*-site ionic displacements (AFE/FE) and the octahedral rotation (AFD) mode(s). In this paper, *in situ* neutron-powder diffraction has been employed to investigate the structural evolution of $Pb_{0.99}(Nb_{0.02}Zr_{0.65}Sn_{0.28}Ti_{0.05})O_3$ (PNZST hereafter) ceramics under different *E*-fields and temperatures. By measuring the diffraction peaks associated with the AFE/FE and AFD modes as a function of different external stimuli, the roles of the *A*-site ionic displacements and octahedral rotation are investigated across the AFE-FE phase transition. Additionally, in real PZO-related materials, in particular polycrystalline materials, the preferred orientation as well as the crystal structure play a very important role in determining the material properties [8,32,33]. Therefore, the associated preferred orientation evolution and its impacts on the relative properties during the phase-transition process have also been investigated, and this may lead to a new method to tune the electrical properties.

## II. EXPERIMENTAL METHOD

### A. Sample preparation

The PNZST ceramic samples were prepared by the conventional solid-state reaction. The reagent oxides $Pb_3O_4(99.9\%)$, $ZrO_2(99.9\%)$, $SnO_2(99.9\%)$, $TiO_2(99.6\%)$, and $Nb_2O_5$ (99.9%) were mixed thoroughly in a planetary ball mill for 4 h using ethanol as a medium. The resultant milled powders
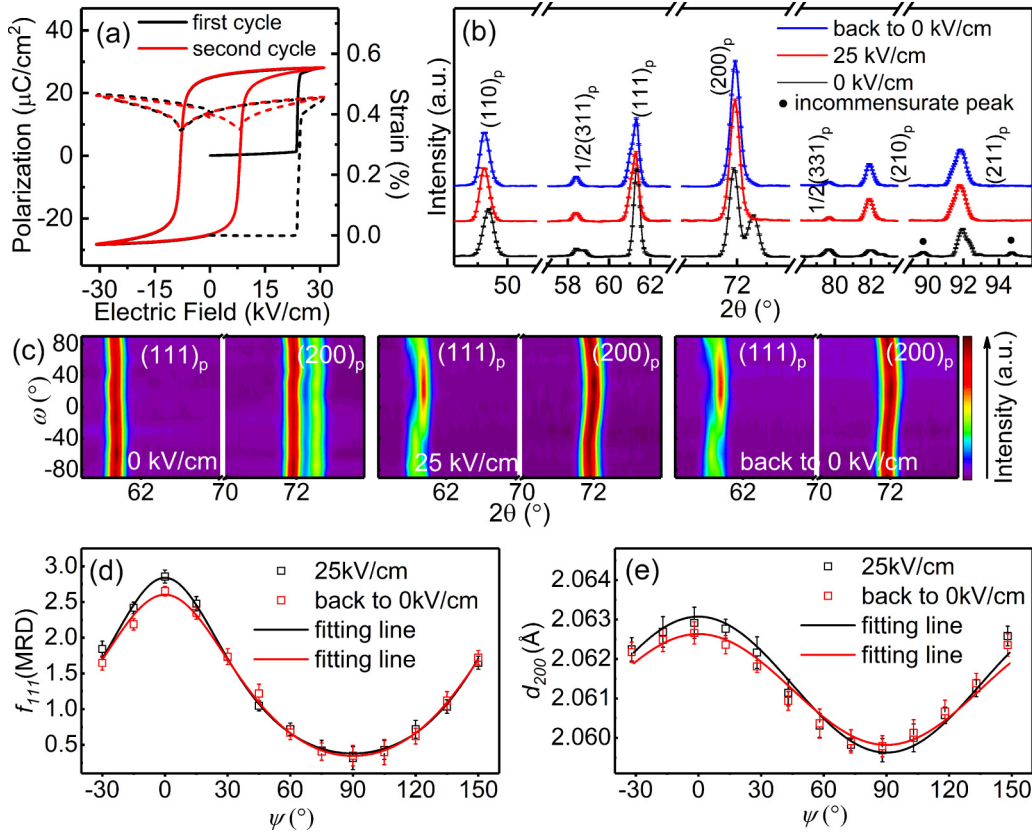
FIG. 2. (a) *P-E* (solid lines) and *S-E* (dashed lines) hysteresis loops of the PNZST ceramic sample at room temperature. (b) *In situ* neutron-diffraction patterns observed at different electric-field points (initial state, 25 kV/cm, and back to 0 field). (c) The $\omega$ dependence of the $(111)_p$ and $(200)_p$ peaks. (d) $f_{111}$(MRD) and (e) $d_{200}$ as a function of the azimuthal angle $\psi$.

were then granulated, pressed into pellets, and sintered at 1300 °C for 1.5 h in a lead-rich environment to minimize lead volatilization, followed by annealing at 860 °C for 6 h to release residual stress resulting from the manufacturing process. Silver paint was then coated onto the pellets' surface and then heat-treated at 550 °C to achieve good electrical contact.

## B. *In situ* neutron diffraction

*In situ* neutron-diffraction patterns (NDPs) were collected on WOMBAT, the high-intensity powder diffractometer at the Australian Nuclear Science and Technology Organisation, with a neutron wavelength of 2.41 Å. The setup was the same as previously reported [8,34]. At room temperature, an external *E*-field was applied normal to the ceramic pellet surface in a sequence of $0 \rightarrow 25 \rightarrow 0$ kV/cm. Then the sample was heated to 398 and 438 K successively. At 438 K, the *E*-field sequence $(0 \rightarrow 20 \rightarrow 0$ kV/cm) was applied to the sample. After the *in situ* high-temperature measurements, the pellet was cooled down to room temperature and its neutron-diffraction patterns were remeasured. At each *E*-field point, the sample was initially set so that the applied field was orthogonal to the incident beam (i.e., at $\omega = -90°$, where $\omega$ is the angle between the incident beam and the applied *E*-field). The sample was then rotated anticlockwise from $\omega = -90°$ to $+90°$ in-plane at an increment of 15°. In total, 13 patterns were collected for each point.

## C. Electrical properties

The pristine ceramic pellet was initially exposed to an *E*-field of 30 kV/cm for 15 min at room temperature in silicone oil. Then the temperature-dependent dielectric spectra of the poled sample were measured as a function of frequencies, $f$, ranging from $1 \leqslant f \leqslant 200$ kHz using a precision LCR meter (Agilent, 4980A). The *P-E* and strain-electric field (*S-E*) hysteresis loops at different temperatures were collected by a TFAnalyzer 2000 with an aixACCT FE test unit, a laser interferometer, and a temperature controller.

## III. RESULTS AND DISCUSSION

### A. Electric-field-induced phase transition at room temperature

The measured, room-temperature, *P-E* (solid lines), and *S-E* (dashed lines) hysteresis loops for the first and second electric cycles are shown in Fig. 2(a). The *P-E* loop shows a linear relationship during the first quarter cycle, corresponding to the typical AFE behavior, until the applied *E*-field reaches $\sim$24 kV/cm. After this critical field, the polarization increases abruptly from near zero to 35 $\mu$C/cm$^2$. The following *P-E* hysteresis loop behaves as a typical FE hysteresis loop with a coercive field ($E_C$) $\sim$ 8.3 kV/cm and a remnant polarization ($P_r$) $\sim$ 30 $\mu$C/cm$^2$. Similar to the *P-E* behavior, no evident change is observed for the longitudinal strain before reaching the critical *E*-field $\sim$24 kV/cm. Then a sudden jump to $\sim$0.45% occurs. However, residual strain was measured even with

the $E$-field reduced to zero where $\sim 0.41\%$ strain remained. This irreversible behavior is in good agreement with the irreversible $E$-field-induced AFE-to-FE phase transition, i.e., the induced FE phase remains metastable after withdrawal of the field [35].

*In situ* NDPs under different $E$-fields are shown in Fig. 2(b), which is obtained by integrating the data taken at all $\omega$ values. All patterns were indexed with respect to the underlying parent perovskite substructure (labeled with subscript p). Before exposure to an $E$-field, the unambiguous 2:1 splitting of the $\langle 200 \rangle_p^*$ peaks (into a $[200]_p^* \equiv [020]_p^*$ peak and a $[002]_p^*$ peak) in conjunction with a nonsplit and symmetric $\langle 111 \rangle_p^*$ peak is indicative of a pseudotetragonal average structure, with the primitive unit-cell lattice parameter relationship $a_p = b_p > c_p$. In addition to the strong parent Bragg reflections $\mathbf{G}_p$, a series of weaker $\mathbf{G}_p \pm 1/2\,[111]_p^*$-type satellite reflections, including $1/2\langle 311 \rangle_p^*$, $1/2\langle 331 \rangle_p^*$, and $1/2\langle 511 \rangle_p^*$, were also observed. Note that the $1/2\langle 311 \rangle_p^*$ peak is clearly split (into a $1/2\,[311]_p^* \equiv 1/2\,[131]_p^*$ peak and a $1/2\,[113]_p^*$ peak). These satellite reflections result from the aforementioned condensed $\mathbf{q}_2$ mode associated with $a^-a^-c^0$ ZrO$_6$ octahedral tilting, which is a typical feature of PZO and doped-PZO AFE materials [21,36].

Two additional peaks near the $\langle 211 \rangle_p^*$ Bragg reflection can be attributed to $\mathbf{G}_p \pm \gamma [110]_p^*$-type satellite reflections, which are related to the AFE mode with the incommensurate modulation wave-vector mentioned above [29,36]. As shown in Figs. 1(a) and 1(c), these satellite reflections suggest the existence of $(010) \equiv (110)_p$ ferroelectric slabs of average width $1/2\gamma [110]_p$, alternately polarized up and down along the $\boldsymbol{a} \equiv [1\text{-}10]_p$ direction, respectively.

Upon increasing the field to 25 kV/cm (exceeding the critical $E$-field corresponding to the abrupt changes in polarization and strain as described above), the initially split $\langle 200 \rangle_p^*$ peaks merge together into a single peak while the initially unsplit $\langle 111 \rangle_p^*$ peak develops a low-angle shoulder, consistent with a change to rhombohedral symmetry. This is also consistent with the initially split $1/2\langle 311 \rangle_p^*/1/2\langle 113 \rangle_p^*$ peaks merging together into a single peak. The other $\mathbf{G}_p \pm 1/2[111]_p^*$-type satellite reflections are still apparent, but the two $\mathbf{G}_p \pm \gamma [110]_p^*$ satellite peaks associated with the AFE mode disappear altogether. The unsplit $\mathbf{G}_p \pm 1/2[111]_p^*$-type satellite reflections are consistent with the presence of $a^-a^-a^-$ octahedral tilting. In summary, these observations are consistent with an AFE to rhombohedral FE (FE$_R$) phase transition. The space-group symmetry of this field-induced FE$_R$ phase is assigned to rhombohedral $R3c$. Similar to the initial AFE structure, the FE$_R$ structure is also dominated by two strong modes. One is the zone center FE mode, $\mathbf{q} = [000]_p^*$, with off-center Pb$^{2+}$ and O$^{2-}$ displacements along the unique $[111]_p$ direction. The other is the AFD, $\mathbf{q}_2 = 1/2[111]_p^*$ mode, now corresponding to $a^-a^-a^-$ octahedral tilting rather than the $a^-a^-c^0$ octahedral tilting in the AFE phase. After withdrawal of the $E$-field, the NDP remains the same as that observed at 25 kV/cm, demonstrating that the induced FE$_R$ phase becomes metastable and the field-induced AFE to FE$_R$ phase transition is irreversible, in accordance with the ferroelectric properties measurements.

Considering our focus in this work is the evolution of the average structure as well as the strain and preferred orientation during the phase transition, the primitive unit-cell parameters for different phases are calculated by fitting the corresponding NDPs using Jana2006 [37]. To accommodate $a^-a^-c^0$ octahedral tilting, the lattice parameters of the AFE phase were refined to an orthorhombic structure with $\boldsymbol{a} = \boldsymbol{a}_p - \boldsymbol{b}_p, \boldsymbol{b} = \boldsymbol{a}_p + \boldsymbol{b}_p$, and $\boldsymbol{c} = 2\boldsymbol{c}_p$ [illustrated in Fig. 1(b)] while the $R3c$ symmetry was adopted to the FE$_R$ phase. After Le-Bail fitting the NDPs collected at 0 and 25 kV/cm, the primitive unit-cell parameters were $a_p = 4.1240(5)$ Å and $c_p = 4.0916(5)$ Å for the AFE phase [although the angle between $\boldsymbol{a}_p$ and $\boldsymbol{b}_p$ is $89.89(4)°$], and $a_r = 4.1221(5)$ Å and $\alpha_r = 89.83(4)°$ for the FE$_R$ phase in the rhombohedral setting.

According to the primitive unit-cell parameters of both AFE and FE$_R$ phases, it is evident that the phase transition from AFE to FE$_R$ can generate a large volume expansion. Additionally, the development of the preferred orientation also contributes to the strain ($\sim 0.45\%$) observed during the first quarter $E$-field cycle. Figure 2(c) shows NDPs of two selected "peak" regions ($\langle 111 \rangle_p^*$ and $\langle 200 \rangle_p^*$) as a function of $\omega$ angles corresponding to different $E$-fields. Before applying the $E$-field, no $\omega$ dependence was observed on both the peak positions and intensities of the split $\langle 200 \rangle_p^*$ peaks and $\langle 111 \rangle_p^*$ peak. When the sample transfers into the FE$_R$ phase with a 25 kV/cm $E$-field, the initially split $\langle 200 \rangle_p^*$ peaks merge together into one single peak while the peak position shows an S-shaped trajectory as a function of $\omega$ value. Furthermore, the intensities of the now split $[111]_p^*$ and $[11\text{-}1]_p^*$ peaks show a strong dependence on $\omega$, indicating a strong preferred orientation formed during the phase transition. After withdrawal of the $E$-field, no significant change could be observed in the $\omega$-dependent NDPs. For further analysis of this preferred orientation and the lattice strain observed in the metastable FE state, the parameters $d_{200}$ and $f_{111}$(MRD) are used, where MRD means multiple random distribution [33,38]:

$$f_{111}(\mathrm{MRD}) = 4\left(\frac{I_{111}}{I'_{111}}\right)\Bigg/\left[\frac{I_{111}}{I'_{111}} + 3\left(\frac{I_{11\bar{1}}}{I'_{11\bar{1}}}\right)\right], \quad (1)$$

where $I$ denotes the relevant peak intensity, calculated by multipeak fitting using two pseudo-Voigt profiles, while $I'$ is the relevant peak intensity corresponding to a sample with random orientation. The values of $I'$ are obtained by averaging the observed intensities over all 13 measured patterns. Instead of the rotation angle $\omega$, the azimuthal angle $\psi$, where $\psi = \omega - \theta_{hkl} + 90°$ [$\theta_{hkl}$ is the Bragg angle for particular ($hkl$) reflection], is used to clearly demonstrate the distribution of the preferred orientation. The calculated value of $f_{111}$(MRD) as a function of $\psi$ is shown in Fig. 2(d) and can be well fitted by a revised elliptical function used in the previous study of the preferred orientation (both $\psi$-dependent $I_{111}$ and $I_{11\text{-}1}$ can be fit to the elliptical function) [8]. As the polar axis of the FE$_R$ phase is along the $[111]_p$ direction, after exposure to the $E$-field the volume of the domain along the $[111]_p$ direction becomes maximum parallel to the $E$-field.

The formation of this preferred orientation contributes strongly to the longitudinal expansion in the PNZST sample. After withdrawal of the $E$-field, relaxation of this preferred orientation is almost negligible, suggesting less recoverable strain from non-180° domain back-switching. In addition to
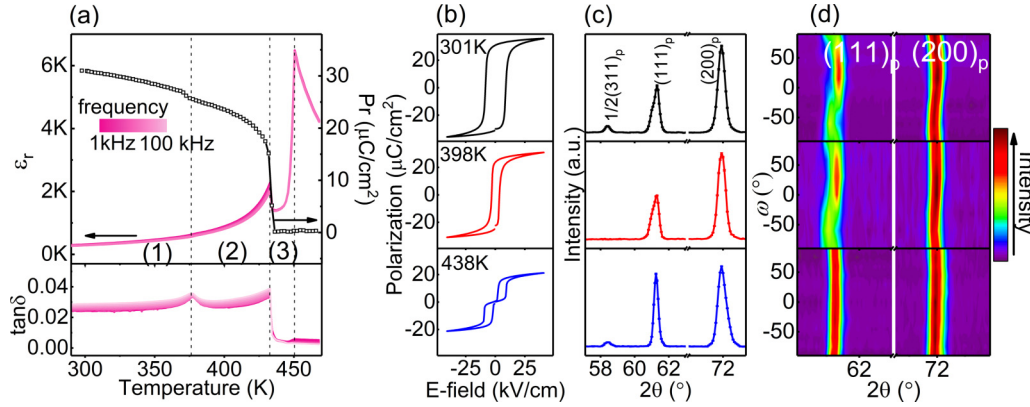
FIG. 3. (a) Temperature-dependent dielectric spectra and the spontaneous polarization of the poled PNZST sample from 290 to 470 K. (b) The *P-E* hysteresis loops, (c) average NDPs and (d) $\omega$-dependent NDPs of the poled PNZST sample at selected temperature points.

the formation of the preferred orientation, large lattice strains are also obtained during this process [Fig. 2(e)]. The measured $d_{200}$-$\psi$ relation follows very well the elliptical function used before [8]:

$$d_{200} = d_{200}^{\max}\cos^2\psi + d_{200}^{\min}\sin^2\psi. \quad (2)$$

It is also apparent that $d_{200}$ shows a strong expansion in the direction parallel to the *E*-field, contributing to the macroscopic 0.45% expansion along the longitudinal direction. Finally, upon returning to zero field, the relaxation of the lattice strain is also weak, suggesting a large residual strain is stored in the metastable FE$_R$ phase.

During the *E*-field-induced AFE-FE phase transition at room temperature, obviously both AFE and FE phases contain AFD modes but in different forms. The $a^-a^-c^0$-type tilting remains in the AFE phase. Referring to the calculation results [14,39], this type of tilting is coupled with the AFE mode associated with the $\mathbf{q} = [uu0]_p^*$ modulation wave vector, which in our case is the $\mathbf{q_1} = \gamma[110]_p^*$ incommensurate structure mode. The induced FE$_R$ phase presents $a^-a^-a^-$-type octahedral tilting, while none of the AFE mode can be deduced from the calculation for this kind of tilting, and only the zone-center FE mode can be coupled with this rotation mode [14].

### B. Temperature-induced phase transition

As shown by the room-temperature *P-E* hysteresis loop and *in situ* neutron-diffraction results, the sample will remain in the FE$_R$ state at room temperature after exposure to an *E*-field at or above 25 kV/cm. When this metastable FE$_R$ state is heated, it experiences a sequence of phase transitions. Figure 3(a) shows the temperature-dependent dielectric spectra and remnant polarization ($P_r$) of the poled sample. Two obvious peaks in the dielectric constant appear around 432 and 450 K, respectively. The dielectric loss spectrum shows an obvious change around 376 K, at which temperature no abrupt variation in the dielectric constant occurs. The $P_r$ versus temperature curve has a small discontinuous drop around 376 K before an abrupt decrease to zero around 432 K. The variation in temperature-dependent dielectric properties and $P_r$ shows that the poled PNZST sample experiences at least two phase transitions before entering the paraelectric phase. Figure 3(b) shows *P-E* hysteresis loops at three different temperatures

corresponding to the three typical regions in Fig. 3(a). In both regions (1) and (2), the sample exhibits a single *P-E* hysteresis loop, suggesting that the dielectric anomaly around 376 K is possibly related to a phase transition between two FE phases (note that the three *P-E* hysteresis loop measurements are single-loop measurements without a prepoling pulse). The small change in spontaneous polarization and a peak in dielectric loss are consistent with the disappearance of the $a^-a^-a^-$ ZrO$_6$ octahedral rotation, as reported previously in several studies [40–42].

Upon increasing the temperature to 432 K, the observed $P_r$ declines sharply to zero. In temperature region (3), the sample shows a typical double *P-E* hysteresis loop [see the bottom panel of Fig. 3(b)]. This behavior indicates that the depolarization process occurring around 432 K is associated with a FE-AFE phase transition. Figure 3(c) shows the corresponding neutron-diffraction patterns. At 301 K, the poled sample is still in the metastable FE$_R$ phase. When heated to 398 K, the split $\langle111\rangle_p^*$ peaks are still obvious, but no trace of the $1/2\langle331\rangle_p^*$ peak(s) or other $\mathbf{G}_p \pm 1/2\,[111]_p^*$-type reflections can be obtained. In other words, the amplitude of the AFD mode effectively goes to zero at this temperature, denoting that the initially ordered octahedral rotation becomes significantly disordered, and hence unobservable due to the higher thermal energy. The NDPs further support the interpretation that the dielectric loss and $P_r$ responses occurring at 376 K are thus attributed to a low-temperature FE ($R3c$) to high-temperature FE ($R3m$) phase transition. In the high-temperature FE phase, the $A$-site ionic shifts and octahedral tilting become decoupled, in the sense that the FE, $\mathbf{q} = [000]_p^*$ mode still remains nonzero in the complete absence of the $\mathbf{q_2} = 1/2\,[111]_p^*$ octahedral rotation mode. Even if these two modes become formally independent above 376 K, the small drop of $P_r$ around 376 K indicates a weak coupling between the $\mathbf{q} = [000]_p^*$ and $\mathbf{q_2} = 1/2\,[111]_p^*$ modes for the low-temperature FE phase, consistent with the previous research on lead zirconate titanate [40].

Upon further increasing temperature to 438 K, the initially split $\langle111\rangle_p^*$ peaks merge together to form a single and symmetric peak. At the same time, the $\langle200\rangle_p^*$ peak becomes broader and asymmetric with a shoulder at higher angle, in accordance with the pseudotetragonal AFE structure. Additionally, the $1/2\langle331\rangle_p^*$ peaks reappear and the
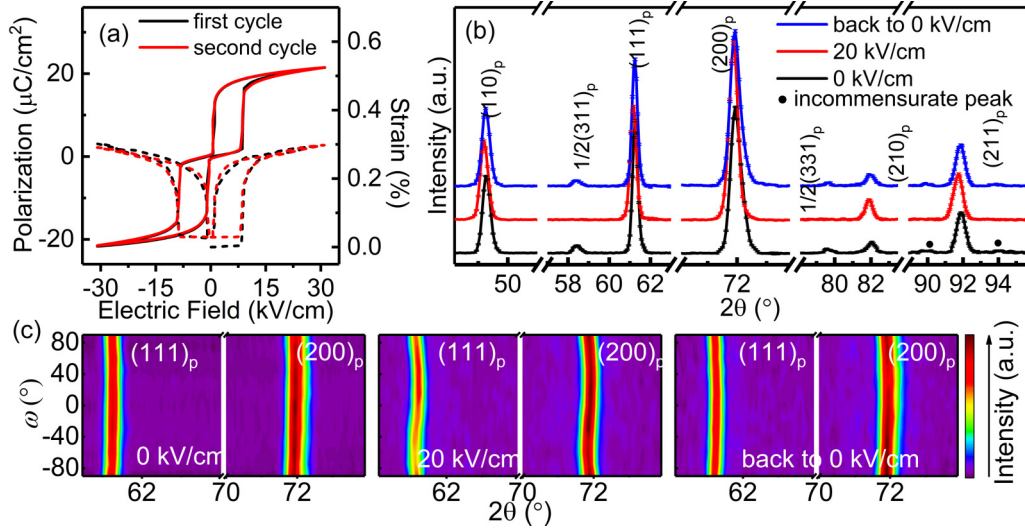
FIG. 4. (a) *P-E* (solid lines) and *S-E* (dashed lines) hysteresis loops of the PNZST ceramic sample at 438 K. (b) *In situ* neutron-diffraction patterns observed at different electric-field points (initial state, 20 kV/cm, and back to 0 field). (c) The $\omega$ dependence of the $(111)_p$ and $(200)_p$ peaks.

diffraction pattern becomes quite similar to that observed for the original AFE phase, consistent with the proposition that a FE-to-AFE phase transition occurs around 432 K. During this process, the amplitude of the $\mathbf{q} = [000]_p{}^*$ FE mode goes to zero, leading to the abrupt increase in the temperature-dependent dielectric spectra and the zero $P_r$. It is interesting to note the condensation of the $\mathbf{q}_2 = {}^1/_2[111]_p{}^*$ mode at high temperature. The simultaneous reappearance of the octahedral rotation and the antiparallel ionic displacements further supports the fact that the strong coupling between the AFE and AFD modes contributes to the AFE structure and the antiferroelectricity described by the first-principles calculation [17].

The $\omega$-dependent NDPs [see Fig. 3(d)] show the variation in preferred orientation during the temperature-induced phase transitions in a poled PNZST sample. The preferred orientation at 301 K is the same as that analyzed in the previous section. When the low-temperature FE phase transfers into the high-temperature FE phase, no obvious change can be observed in the $\omega$-dependent NDPs, i.e., the FE $[111]_p$ direction still prefers to align parallel to the *E*-field. This is also the reason that the origin of the polarization starts from $-25\,\mu C/cm^2$ rather than zero when measuring the *P-E* hysteresis loop at 398 K. This phenomenon suggests that the destabilization of the octahedral rotation in the FE phase does not strongly influence the redistribution of the non-180 domains. Upon further increasing the temperature to trigger the FE-to-AFE phase transition, the structure changes from rhombohedral to pseudotetragonal. Both the positions and intensities of the $\langle 111 \rangle_p{}^*$ and $\langle 200 \rangle_p{}^*$ peaks revert to unchanged as the pellet sample is rotated. That is, during the temperature-induced FE-to-AFE phase transition, the grain orientation returns to an isotropic distribution, essentially identical to the original AFE state.

## C. Electric-field-induced phase transition at high temperature

As mentioned earlier, when the temperature is in the range of 430–450 K, the poled sample reverts to the AFE phase.

Figure 4(a) shows *P-E* (solid lines) and *S-E* (dashed lines) hysteresis loops at $T = 438$ K. The observed double *P-E* hysteresis loop suggests that the PNZST sample shows a reversible AFE-FE phase transition at this temperature, i.e., the macroscopic polarization exhibits a sudden increase when the applied *E*-field is larger than 10 kV/cm and returns to zero after withdrawal of the field. Although the observed *P-E* behavior is almost the same during the first and second cycles, the *S-E* loops show a slight difference.

Figure 4(b) shows *in situ* NDPs taken at 438 K. Before applying the external field, note that the $\langle 200 \rangle_p{}^*$ peak is quite broad and asymmetric due to a small shoulder at a higher $2\theta$ angle, while the $\langle 111 \rangle_p{}^*$ peak is much narrower and more symmetric. In addition to these parent reflections, the same $\mathbf{G}_p \pm 1/2\,[111]_p{}^*$ satellite reflections as that at room temperature in the absence of an *E*-field are again evident. The incommensurate peaks associated with the AFE mode can still be observed even though they have now broadened noticeably. The diffraction data at this elevated temperature are thus quite consistent with that of the AFE structure at room temperature.

Upon applying an *E*-field of 20 kV/cm, the broadness and asymmetry of the $\langle 200 \rangle_p{}^*$ peak disappear while the $\langle 111 \rangle_p{}^*$ peak appears to remain unsplit, indicating the formation of a new phase with metric cubic symmetry. However, the fact that the measured polarization rises steeply up to $15\,\mu C/cm^2$ after an applied *E*-field exceeding the critical value $\sim 10$ kV/cm requires the structure of the phase obtained under an *E*-field of 20 kV/cm to be a FE structure, presumably with lower than cubic symmetry. The disappearance of the $\mathbf{G}_p \pm 1/2\,[111]_p{}^*$ satellite reflections under the applied *E*-field suggests the disappearance of octahedral tilting during the *E*-field-induced AFE-FE phase transition. This indicates that the high-temperature, field-induced FE phase belongs to the *R*3*m* structure described in the PNZST phase diagram [23]. When the applied field returns to zero, the NDP reverts to the same state as that observed initially, consistent with a reversible AFE-FE phase transition characterized by the double *P-E* hysteresis loop.
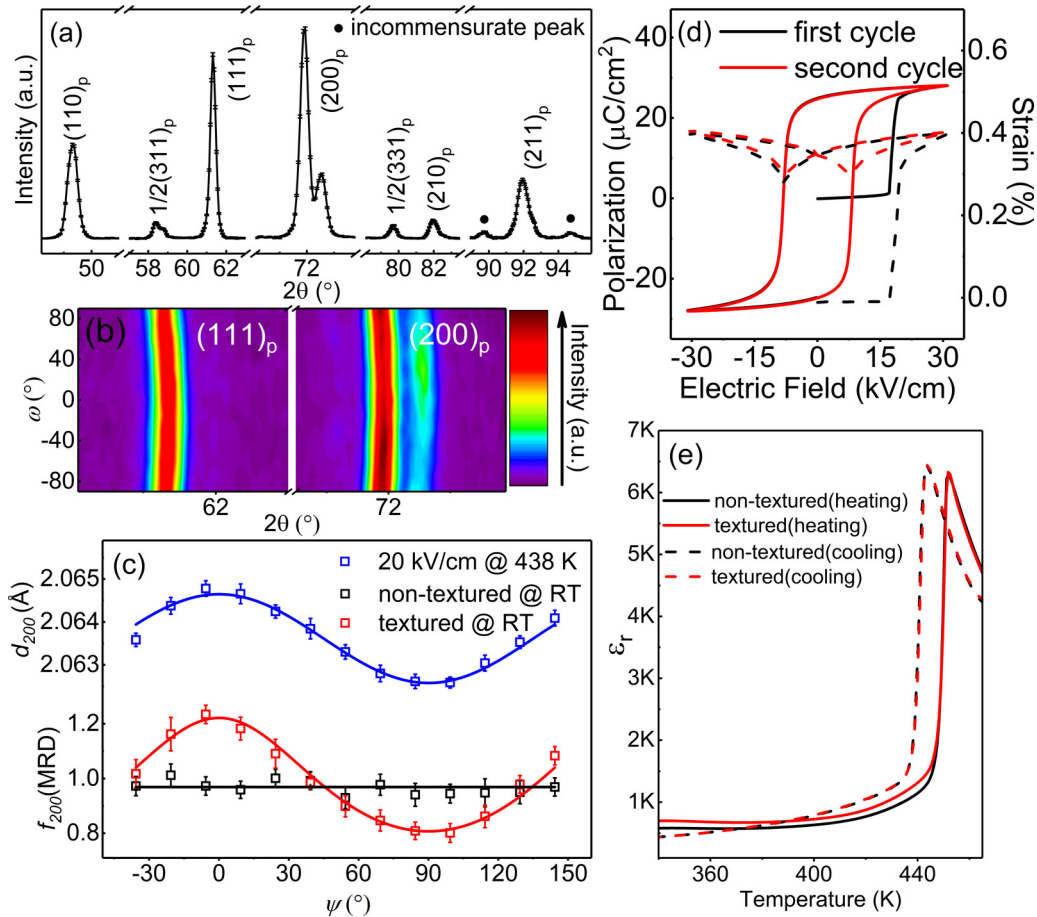
FIG. 5. Room-temperature (a) average and (b) $\omega$-dependent NDPs of the sample, which has been exposed to an external field at 438 K. (c) $d_{200}$ as a function of the azimuthal angle, $\psi$, for the induced FE state at 438 K (with applying 20 kV/cm) and the $f_{200}$(MRD)-$\psi$ curves for the virgin PNZST sample (black) and textured sample (red) at room temperature. Note that the solid line is the fitting line. (d) *P-E* (solid lines) and *S-E* (dashed lines) hysteresis loops of the textured PNZST ceramic sample at room temperature. (e) The temperature-dependent dielectric spectra for nontextured (black) and textured (red) AFE PNZST samples during the heating (solid lines) and cooling (dot-lines) process, measured at 10 kHz.

The primitive unit-cell lattice parameters were calculated to be $a_p = 4.1255(5)$ Å and $c_p = 4.1123(5)$ Å for the AFE phase, and $a_r = 4.1274(5)$ Å and $\alpha_r = 89.89(6)°$ for the induced FE phase. Comparison with the room-temperature values shows that the AFE phase exhibits thermal expansion with the $c_p$ parameter expanding significantly more quickly ($\sim 0.51\%$) while the $a_p$ parameter barely expands at all ($\sim 0.03\%$), in accordance with previous temperature-dependent diffraction studies [43]. Note that the refined $a_p$ and $c_p$ parameters at high temperature are closer to the refined $a_r$ parameter of the induced FE phase. This most likely facilitates the reversible AFE-FE phase transition at high temperature but not at room temperature. Figure 4(c) shows the $\omega$ dependence of the $\langle 111 \rangle_p{}^*$ and $\langle 200 \rangle_p{}^*$ peaks at three different electric-field points. For the initial AFE state, both the peak positions and peak widths of the $\langle 111 \rangle_p{}^*$ and $\langle 200 \rangle_p{}^*$ peaks are independent of the rotation angle $\omega$. In the FE state, the peak positions of both the $\langle 111 \rangle_p{}^*$ and $\langle 200 \rangle_p{}^*$ peaks exhibit typical S-shaped trajectories as a function of $\omega$, characteristic of preferred orientation as described above for the field-induced FE phase at room temperature. Note also that this time, the $\langle 111 \rangle_p{}^*$ peak does not split into two peaks as a function of $\omega$.

Finally, for the AFE phase recovered from the induced FE phase, the shape of the $\langle 200 \rangle_p{}^*$ peak behaves differently from that observed in the initial AFE state. Over the $\omega$ value range from $-20°$ to $40°$, the peak width is broadened relative to that obtained at other $\omega$ values. In addition, the intensity of the $\langle 200 \rangle_p{}^*$ peak seems to have a minimum value around $\omega = 40°$ and a maximum value around $\omega = -60°$, suggesting the formation of preferred orientation after the reversible AFE-FE phase transition. This phenomenon is consistent with our previous report on a closely related system [8]. Because the $\langle 200 \rangle_p{}^*$ peaks at high temperature do not present evident splitting, it is difficult to reliably calculate $f_{200}$(MRD), necessary as an index for the domain fractions along the $\boldsymbol{a}_p$ and $\boldsymbol{c}_p$ directions. Upon cooling the sample to room temperature, there is no obvious difference between the average structure observed after experiencing the above experimental sequence and that of the virgin sample [see Fig. 5(a)], but the preferred orientation induced at high temperature has been stored [see Fig. 5(b)].

By contrast with the broad and asymmetric $\langle 200 \rangle_p{}^*$ peak at high temperature, after cooling to room temperature the $\langle 200 \rangle_p{}^*$ peak splits into two peaks with the relative intensities of this doublet showing a clear dependence on $\omega$. Starting

TABLE I. Summary of the *in situ* neutron-diffraction results carried on the PNZST samples. The experimental sequence suggests that the sample state is decided by previous experiments.

| Experimental sequence | Temperature (K) | Electric field (kV/cm) | Sample phase | Dominated modes | Preferred orientation |
|---|---|---|---|---|---|
| 1 | 301 | 0 | AFE | AFE + AFD | No |
| 2 | 301 | 25 | FE | FE+ AFD | Yes |
| 3 | 301 | 0 | FE | FE+ AFD | Yes |
| 4 | 398 | 0 | FE | FE | Yes |
| 5 | 438 | 0 | AFE | AFE + AFD | No |
| 6 | 438 | 20 | FE | FE | Yes |
| 7 | 438 | 0 | AFE | AFE + AFD | Yes |
| 8 | 301 | 0 | AFE | AFE + AFD | Yes |

from the $+\omega$ side (in the vicinity of 90°), the intensity of the $([200]_p{}^*, [020]_p{}^*)$ peak (on the low $2\theta$ side) is strong while that of the $[002]_p{}^*$ peak is weak. Upon decreasing $+\omega$ to 30°, however, the $[002]_p{}^*$ peak on the high-angle side becomes much stronger while the intensity of the $([200]_p{}^*, [020]_p{}^*)$ peak decreases. Upon further decreasing $\omega$ to the $-\omega$ side, the intensity of the $[002]_p{}^*$ peak gradually drops down until $\omega = -60°$ while the intensity of the $([200]_p{}^*, [020]_p{}^*)$ peak follows the opposite trend, i.e., the maximum of $I_{200}$ appears when $\omega$ is around $-60°$. Figure 5(c) shows the details about the formation of preferred orientation at room temperature. The $d_{200}$ value of the induced FE phase at 438 K shows a strong dependence on $\psi$, and the data could be fitted well using Eq. (2). Note that the maximum value of $d_{200}$ appears parallel to the *E*-field. The $f_{200}$(MRD) was calculated as follows:

$$ f_{200}(\text{MRD}) = 3 \left( \frac{I_{200}}{I'_{200}} \right) \bigg/ \left[ \frac{I_{200}}{I'_{200}} + 2 \left( \frac{I_{002}}{I'_{002}} \right) \right]. \tag{3} $$

Again, the maximum value of $f_{200}$ appears parallel to the *E*-field. These results further support the proposition reported above that the elastic strain observed in the induced FE phase drives the preferred orientation distribution during the reversible AFE-FE phase transition [8]. As the *a/c* domains have already nucleated in the AFE phase at high temperature, they will grow along their preferred orientation during the cooling process.

Figure 5(d) shows *P-E* (solid lines) and *S-E* (dashed lines) hysteresis loops of the textured sample, suggesting that the AFE phase experiences a steplike transition into the FE phase at $E \sim 18$ kV/cm while afterward the system displays a "classical" ferroelectric hysteresis loop. Although the general behavior of the textured AFE phase is similar to that of the nontextured one [Fig. 1(a)], there are a few features that show a slight divergence, e.g., (i) the critical field to trigger the irreversible AFE-FE phase transition is ∼25 kV/cm in the nontextured sample and 18 kV/cm in the textured sample, and (ii) the maximum strain measured at 30 kV/cm is ∼0.45% in the nontextured sample and ∼0.40% in the textured sample.

Finally, Fig. 5(e) displays the temperature-dependent dielectric spectra of the textured and nontextured samples during the heating and cooling process. It is evident that for the nonpoled sample, only one dielectric anomaly, corresponding to the AFE-to-PE phase transition, can be observed in this temperature range. The textured sample shows a larger

dielectric constant. After transferring into the paraelectric phase, the crystallographic texture disappears so that during the cooling process the dielectric constants of the textured and nontextured samples overlap. The variation in properties between the textured and nontextured samples further suggests that, in addition to the average structure, the preferred orientation of polycrystalline materials has a strong impact on their properties.

## IV. CONCLUSION

The study of *in situ* neutron diffraction of polycrystalline PNZST samples, together with the associated electrical property characterization, presents a clear picture of the evolution of the AFE, FE, and AFD modes and preferred orientation with respect to *E*-field and/or temperature. The details are summarized in the Table I.

The room-temperature *E*-field-induced irreversible AFE-FE phase transition is in accordance with the calculation results that the different kinds of octahedral rotation will comply with different kinds of *A*-site ionic shifts, i.e., the $a^-a^-c^0$ tilting system prefers to be coupled with the AFE mode associated with the $[uu0]_p{}^*$ modulation wave vector while the $a^-a^-a^-$ tilting is only happy to be coupled with the zone-center FE mode. During the temperature-induced FE ($R3c$) to FE ($R3m$) to AFE phase transitions, the AFD mode is first decoupled with the FE mode, i.e., the amplitude of the $a^-a^-a^-$ tilting mode drops to zero with increasing thermal energy. Additionally, the small change in $P_r$ indicates that the coupling between the FE and AFD modes in FE ($R3c$) is quite weak. Upon further increasing the temperature to trigger the FE ($R3m$) to AFE phase transition, interestingly, the simultaneous condensation of AFD and AFE modes further proves the importance of the coupling between AFD and AFE modes in stabilizing the AFE structure, which is indicated by previous calculation results. The high-temperature *E*-field-induced reversible AFE-FE phase transition also supplies evidence that with aligning $Pb^{2+}$ displacements along the same direction by the *E*-field, the $a^-a^-c^0$ octahedral tilting will disappear, but it will reappear together with the AFE mode after withdrawal of the *E*-field. In addition to the average structure, the preferred orientation is also formed and modified during the AFE-FE phase-transition process, and its correlation to the properties has also been developed.

We believe this work firstly addresses the critical role of the coupling between the AFD mode and the AFE mode in stabilizing the AFE structure, and thus establishing a solid interaction between the structure, crystal texture, and properties of AFE materials under different external stimuli and their combination, facilitating the design and development of new AFE materials.

[1] W. Y. Pan, C. Q. Dam, Q. M. Zhang, and L. E. Cross, J. Appl. Phys. **66**, 6014 (1989).

[2] Z. Liu, X. Chen, W. Peng, C. Xu, X. Dong, F. Cao, and G. Wang, Appl. Phys. Lett. **106**, 262901 (2015).

[3] M. S. Mirshekarloo, K. Yao, and T. Sritharan, Adv. Funct. Mater. **22**, 4159 (2012).

[4] J. Ge, D. Remiens, X. Dong, Y. Chen, J. Costecalde, F. Gao, F. Cao, and G. Wang, Appl. Phys. Lett. **105**, 112908 (2014).

[5] F. Zhuo, Q. Li, J. Gao, Y. Wang, Q. Yan, Z. Xia, Y. Zhang, and X. Chu, J. Mater. Chem. C **4**, 7110 (2016).

[6] M. Pešić, M. Hoffmann, C. Richter, T. Mikolajick, and U. Schroeder, Adv. Funct. Mater. **26**, 7486 (2016).

[7] Y. Tian, L. Jin, H. Zhang, Z. Xu, X. Wei, E. Politova, S. Y. Stefanovich, N. V. Tarakina, I. Abrahams, and H. Yan, J. Mater. Chem. A **4**, 17279 (2016).

[8] T. Lu, A. J. Studer, L. Noren, W. Hu, D. Yu, B. McBride, Y. Feng, R. L. Withers, H. Chen, Z. Xu, and Y. Liu, Sci. Rep. **6**, 23659 (2016).

[9] M. Avdeev, J. D. Jorgensen, S. Short, G. A. Samara, E. L. Venturini, P. Yang, and B. Morosin, Phys. Rev. B **73**, 064105 (2006).

[10] Z. Dai, Z. Xu, and X. Yao, Appl. Phys. Lett. **92**, 072904 (2008).

[11] T. Lu, A. J. Studer, D. Cortie, K. Lau, D. Yu, Y. Feng, H. Chen, Z. Xu, R. L. Withers, G. J. McIntyre, and Y. Liu, ACS Appl. Mater. Interf. **8**, 14313 (2016).

[12] L. E. Cross, J. Phys. Soc. Jpn. **23**, 77 (1967).

[13] A. K. Tagantsev, K. Vaideeswaran, S. B. Vakhrushev, A. V. Filimonov, R. G. Burkovsky, A. Shaganov, D. Andronikova, A. I. Rudskoy, A. Q. R. Baron, H. Uchiyama, D. Chernyshov, A. Bosak, Z. Ujma, K. Roleder, A. Majchrowski, J. H. Ko, and N. Setter, Nat. Commun. **4**, 2229 (2013).

[14] L. Bellaiche and J. Íñiguez, Phys. Rev. B **88**, 014104 (2013).

[15] J. Hlinka, T. Ostapchuk, E. Buixaderas, C. Kadlec, P. Kuzel, I. Gregora, J. Kroupa, M. Savinov, A. Klic, J. Drahokoupil, I. Etxebarria, and J. Dec, Phys. Rev. Lett. **112**, 197601 (2014).

[16] J. Íñiguez, M. Stengel, S. Prosandeev, and L. Bellaiche, Phys. Rev. B **90**, 220103 (2014).

[17] K. Patel, S. Prosandeev, Y. Yang, B. Xu, J. Íñiguez, and L. Bellaiche, Phys. Rev. B **94**, 054107 (2016).

[18] P. Tolédano and M. Guennou, Phys. Rev. B **94**, 014107 (2016).

[19] D. Orobengoa, C. Capillas, M. I. Aroyo, and J. M. Perez-Mato, J. Appl. Crystallogr. **42**, 820 (2009).

[20] B. J. Campbell, H. T. Stokes, D. E. Tanner, and D. M. Hatch, J. Appl. Crystallogr. **39**, 607 (2006).

[21] D. L. Corker, A. M. Glazer, J. Dec, K. Roleder, and R. W. Whatmore, Acta Cryst. Sect. B **53**, 135 (1997).

[22] D. Berlincourt, H. H. A. Krueger, and B. Jaffe, J. Phys. Chem. Solids **25**, 659 (1964).

[23] D. A. Berlincourt, IEEE Trans. Son. Ultrason. **13**, 116 (1966).

[24] X. Tan, C. Ma, J. Frederick, S. Beckman, and K. G. Webber, J. Am. Ceram. Soc. **94**, 4091 (2011).

[25] Z. Xu, D. Viehland, P. Yang, and D. A. Payne, J. Appl. Phys. **74**, 3406 (1993).

[26] D. Viehland, D. Forst, Z. Xu, and J.-F. Li, J. Am. Ceram. Soc. **78**, 2101 (1995).

[27] D. Forst, J. F. Li, and Z. K. Xu, J. Am. Ceram. Soc. **81**, 2225 (1998).

[28] H. He and X. Tan, Appl. Phys. Lett. **85**, 3187 (2004).

[29] H. He and X. Tan, Phys. Rev. B **72**, 024102 (2005).

[30] E. Sawaguchi, H. Maniwa, and S. Hoshino, Phys. Rev. **83**, 1078 (1951).

[31] I. A. Kornev, L. Bellaiche, P. E. Janolin, B. Dkhil, and E. Suard, Phys. Rev. Lett. **97**, 157601 (2006).

[32] J. L. Jones, M. Hoffman, and K. J. Bowman, J. Appl. Phys. **98**, 024115 (2005).

[33] A. Pramanick, D. Damjanovic, J. E. Daniels, J. C. Nino, and J. L. Jones, J. Am. Ceram. Soc. **94**, 293 (2011).

[34] J. Wang, Y. Liu, R. L. Withers, A. Studer, Q. Li, L. Norén, and Y. Guo, J. Appl. Phys. **110**, 084114 (2011).

[35] X. Tan, S. E. Young, Y. H. Seo, J. Y. Zhang, W. Hong, and K. G. Webber, Acta Mater. **62**, 114 (2014).

[36] J. S. Speck, M. De Graef, A. P. Wilkinson, A. K. Cheetham, and D. R. Clarke, J. Appl. Phys. **73**, 7261 (1993).

[37] V. Petříček, M. Dušek, and L. Palatinus, Z. Kristallogr. **229**, 345 (2014).

[38] J. L. Jones, E. B. Slamovich, and K. J. Bowman, J. Appl. Phys. **97**, 034113 (2005).

[39] B. Dupé, S. Prosandeev, G. Geneste, B. Dkhil, and L. Bellaiche, Phys. Rev. Lett. **106**, 237601 (2011).

[40] N. Cereceda, B. Noheda, T. Iglesias, J. R. Fernández-del-Castillo, J. A. Gonzalo, N. Duan, Y. L. Wang, D. E. Cox, and G. Shirane, Phys. Rev. B **55**, 6174 (1997).

[41] J. Frantti, S. Ivanov, S. Eriksson, H. Rundlöf, V. Lantto, J. Lappalainen, and M. Kakihana, Phys. Rev. B **66**, 064108 (2002).

[42] C. A. Randall, M. G. Matsko, W. Cao, and A. S. Bhalla, Solid State Commun. **85**, 193 (1993).

[43] Y. Li, Q. Li, Q. Yan, Y. Zhang, X. Xi, X. Chu, and W. Cao, Appl. Phys. Lett. **101**, 132904 (2012).